Journal of Materials Chemistry A

ROYAL SOCIETY OF CHEMISTRY

PAPER

Cite this: *J. Mater. Chem. A*, 2020, **8**, 13742

Improvement of electrodeposited Sb_2Se_3 thin film photoelectroactivity by cobalt grain boundary modification†

Magno Barcelos Costa, [a] Francisco W. S. Lucas [b] and Lucia Helena Mascaro *[a]

Received 19th March 2020
Accepted 22nd June 2020

DOI: 10.1039/d0ta03160g

rsc.li/materials-a

This work presents, for the first time, the effects of cobalt-modification on the photoelectrochemical properties of Sb_2Se_3 thin films. The insertion of Co^{2+} ions caused an increase in the photocurrent, without protecting and catalytic layers, of 2.5 times towards the hydrogen evolution reaction compared with an unmodified film in the same period and minimized the initial photocorrosion of the material. However, other properties such as bandgap and crystalline structure were not altered by the low degree of modification used in this work. Different results led us to infer that the Co^{2+} ions modified the grain boundaries (GBs) of the Sb_2Se_3 films, creating a local and specific GB inversion and causing these improvements observed in the photoelectrocatalytic properties of the modified films.

1. Introduction

The emergence of absorbing materials which are composed of earth-abundant, inexpensive elements with low toxicity, such as Cu_2O,[1,2] Cu_4TiSe_4,[3] Cu_2SnS_3,[4] $CuSbS_2$ (ref. 5–7) and Sb_2Se_3,[8] has led to growing interest in binary and ternary semiconductors due to their great technological relevance and interesting display of optical and electrical properties. In addition to these features, Sb_2Se_3 is also notable for having a single orthorhombic crystalline phase, which is indicative of better defect and phase control compared to other chalcogenides.[9,10] Among other advantages, the material has a low melting point and a high saturated vapor pressure (600 °C and 1200 Pa at 550 °C, respectively),[11] making it easy to obtain thin films by means of thermal sublimation when using Sb_2Se_3 powder.

The use of Sb_2Se_3 thin films in photovoltaic (PV) and photoelectrochemical (PEC) cell applications has provided a new alternative. It presents suitable bandgap energy between 1.10 and 1.17 eV,[10,12] and a high absorption coefficient in the visible spectrum region ($\alpha \geq 10^5$ cm^{-1} for $h\nu > 1.5$ eV)[13] compared to other commonly used absorbers, such as CZTS ($E_g = 1.45$ eV and $\alpha \geq 10^4$ cm^{-1}),[14] Sb_2S_3 ($E_g \approx 1.70$–2.20 eV and $\alpha \geq 10^4$ cm^{-1})[15] and $CuSbS_2$ ($E_g = 1.40$ eV and $\alpha \geq 10^4$ cm^{-1}).[16] Moreover, its orthorhombic crystalline structure, formed by one-dimensional (1D) parallel ribbons $(Sb_4Se_6)_n$, contributes to the decrease of carrier recombination, since there are few dangling bonds in this structure, even in grain contours, and high anisotropic mobility of the carriers along with the ribbons.[17,18] Thus, this model can lead to an improvement of the photocurrent if textured in the appropriate directions.[19] In addition, the distance between these 1D-ribbons is large enough (3.29 Å) to host cations. The introduction of some ions into these spaces may create localized and specific grain boundaries (GBs) that lead to an electric field between the GBs and the bulk of this material, facilitating the spatial separation of photogenerated electrons and holes. For example, Tang *et al.* observed an efficiency enhancement of Sb_2Se_3 solar cells *via* grain boundary inversion created by interstitial incorporation of Cu ions.[20] PV thin film devices of Sb_2Se_3 have been reported in the literature since 2009; recently, Li *et al.* reached a maximum PV conversion efficiency of 9.2%[21,22] with excellent stability. The structure of the device was ZnO:Al/ZnO/CdS/TiO_2/Sb_2Se_3/$MoSe_2$/Mo, where the Sb_2Se_3 layer was obtained by close-spaced sublimation. Many other authors have also reached high levels of efficiency using different deposition methods, such as vapor transport deposition: 7.6% (2018)[23] and 7.5% (2019)[24]; close-spaced sublimation: 7.3% (2020)[25]; sputtering: 6.84% (2020),[26] 6.15% (2020),[27] 6.06% (2019)[28] and 3.35% (2018)[29]; and rapid thermal evaporation: 6.5% (2017)[30] and 5.6% (2015).[17] These results show that Sb_2Se_3 is a promising material for these applications.

In the photoelectrochemical hydrogen production *via* water splitting, low bandgap photoelectrodes (between 0.80 and 1.20 eV) allow high solar-to-hydrogen (STH) conversion rates if properly combined with high bandgap photoelectrodes (1.60–2.00 eV), through a stacked dual-electrode PEC cell.[10,31] The use of n-type semiconductors as high bandgap photoanodes is widely reported in the literature, with TiO_2,[32] α-Fe_2O_3 (ref. 33)

[a]*Department of Chemistry, Federal University of São Carlos, Road Washington Luiz km 235, São Carlos, SP 13565-905, Brazil*

[b]*Department of Chemical and Biological Engineering and Renewable and Sustainable Energy Institute, University of Colorado Boulder, Boulder, Colorado 80309, USA. E-mail: lmascaro@ufscar.br*

† Electronic supplementary information (ESI) available. See DOI: 10.1039/d0ta03160g

and $BiVO_3$ (ref. 34) highlighted because they are materials with low cost and good efficiency.[35] However, the study of p-type semiconductors as low bandgap photocathodes is more limited, where Sb_2Se_3 is again highlighted, either in the cited configuration or in an even simpler one, where only a photoelectrode is used to perform the electrolysis of water.[35] It is worth mentioning that, in most cases, in this latter configuration, it is necessary to apply an external potential to carry out the water splitting. In the case of Sb_2Se_3, many approaches have been used to improve absorber performance. Recently, Cu-doped NiO_x as an effective hole-selective layer and fullerene as a photoelectron transfer promoter allowed high photoelectrochemical performance to be achieved.[36,37] The highest STH conversion was obtained with protected films (generally with CdS and/or TiO_2 layers) associated with cocatalysts such as Pt, MoS_x and RuO_x, achieving high values of photocurrents of around 16–30 mA cm^{-2} at 0 V_{RHE}.[38–40] However, the films without these layers did not show any appreciable photocurrents, yielding values of around 100 μA cm^{-2} or less.[10,40,41] In the work of Liu *et al.*, the band-edge positions of Sb_2Se_3 thin films were characterized by ultraviolet photoelectron spectroscopy (UPS), showing values of −5.35 and −4.15 eV for the valence band maximum (VBM) and conduction band minimum (CBM), respectively,[42] which demonstrates a suitable energetic structure for promoting the hydrogen evolution reaction (HER) (−4.44 eV at pH 0).[43]

Among the various methods of obtaining Sb_2Se_3 thin films, electrodeposition is considered a promising alternative due to its versatility, scalability, low energy consumption, and ease of handling.[44] In addition, as reported in our previous work, the composition was close to stoichiometric (under appropriate conditions), with the control of film thickness and absence of complexing agents resulting in films strongly attached to the substrate.[19,45] Other advantages of this technique include structural control, from the creation of large-scale superstructures to nanoscale microstructures, and the potential for co-deposition of doping elements.[46] Thus, electrodeposition is being increasingly employed in different ways in the production of semiconductor absorber thin films. For example, there are electrodeposited $CuInSe_2$,[47] Cu_2O,[48] Cu_2SnS_3,[49] and $Cu_2(Zn,Sn)S_4$ (CZTS), with an STH conversion efficiency of 1.46% obtained by Jiang *et al.* using the tandem configuration with $BiVO_3$.[50]

From the different approaches used to improve the photoelectrocatalytic properties of thin films, modifying the material with a foreign species is an approach frequently used to influence its properties. For Sb_2Se_3 thin films, some dopants have already been used for different purposes, such as iron,[45,51] magnesium,[51] copper,[20] zinc,[52] bismuth,[53] sulphur,[54] silver[55] and lanthanides such as samarium,[56] lutetium, ytterbium and europium.[57] With these dopants, it was possible to observe beneficial or harmful contributions to the material, such as an increase in the conductivity of the films and the introduction of deep defects (for Fe and Mg doping), change of conductivity type (for Bi, Cu and Zn doping), electrochemical performance improvement due to a change in morphology (for S doping), enhancement of the crystallinity and increase of the grains (for Ag doping), gain in electrical conductivity (for Sm doping) and promotion of thermoelectric conductivity (for Lu, Yb, and Er doping), respectively.

Herein, this work shows for the first time, as far as we know, the effects of cobalt-modification on the photocurrent response of Sb_2Se_3 obtained by electrodeposition and without protecting and catalytic layers. We present a film in which there was an improvement in stability and photocurrent 2 to 3 times greater than that reported in the literature. Since several transition metal chalcogenides present good semiconductor and electrocatalytic properties, and the Co–Se system is among the least investigated, we chose cobalt as a potential element to achieve this perspective.[58] Several studies have already reported improvements in the catalytic properties of materials applied to photodegradation,[59] hydrogen production[60] and oxygen reduction and evolution[61] upon cobalt incorporation in a different matrix. In 2014, Carim *et al.* obtained amorphous cobalt selenide by electrodeposition and verified potential applications in the HER, exhibiting its good stability and significant catalytic activity.[62] Sb_2Se_3 films with greater photocurrent, morphology control, and easy synthesis process can be applied with better performance in photovoltaic systems, PEC cells for water splitting, and photodegradation of organic molecules. Therefore, from these perspectives presented, it is pertinent to study the cobalt-modification effect on Sb_2Se_3 thin films as a precursor to PEC cells for water splitting using heterojunctions and co-catalysts. The evaluation of the influence of Co on the morphological, structural, optoelectronic and photoelectrocatalytic properties of this material is very important.

2. Experimental section

2.1. Materials and reactants

Selenium oxide (SeO_2, Alfa Aesar, >99.4%); antimony and potassium tartrate ($K_2(SbO)_2C_8H_4O_{10}\cdot xH_2O$, Sigma-Aldrich, >99%); sodium sulphate (Na_2SO_4, Sigma-Aldrich, >99.9%); cobalt sulphate ($CoSO_4\cdot 7H_2O$, Synth, >99%); sulfuric acid (H_2SO_4, Aldrich, 98%); selenium powder (Se, Vetec, >99.9%); fluorine-doped SnO_2-coated glass (FTO, MTI Corporation – 7 ohm $sq.^{-1}$); and argon (Ar, Linde, 99.999%) were used.

2.2. Substrate preparation

The substrate used was FTO, which was cut into pieces (1.5 cm × 1.0 cm). First, they were ultrasonicated in deionized water, ethanol, acetone and isopropanol, for 5 min in each solvent. Subsequently, the FTO plates were hydrophilized at 70 °C for 1 h in a solution of $H_2O/H_2O_{2(conc.)}/NH_4OH_{(conc.)}$, in a ratio of 5 : 1 : 1, respectively. Finally, the plates were rinsed with deionized water and dried in N_2.

2.3. Film deposition

All electrochemical measurements were performed on a Metrohm-Eco Chemie potentiostat/galvanostat (Autolab PGSTAT 302N) using a conventional three-electrode cell. For the working electrode (WE), the counter electrode (CE), and the reference electrode (RE), FTO substrates (geometric area of *ca.* 1 cm^2), Pt

plates (1 cm^2), and a $Ag/AgCl/Cl^-_{(sat.\ KCl)}$ electrode were used, respectively.

For electrodeposition of cobalt-modified Sb_2Se_3 films, the bath was composed of 2.0 mmol L^{-1} H_2SeO_3 and 2.5 mmol L^{-1} SbO^+, as precursors of selenium and antimony, respectively, and $CoSO_4 \cdot 7H_2O$ in Co : Sb proportions of 1 : 20, 1 : 5 and 1 : 2, relative to the antimony concentration, *i.e.*, 0.125, 0.500 and 1.250 mmol L^{-1} of the Co precursor. All reagents were dissolved in 0.5 mol L^{-1} Na_2SO_4/H_2SO_4 – pH 2. One sample was left without $CoSO_4$ and treated as a blank (unmodified film). Each bath solution was pre-deaerated with a N_2 flow for 15 min before the deposition.

The films were obtained through potentiostatic co-electrodeposition, applying a potential of −0.60 V *vs.* $Ag/AgCl/Cl^-_{(sat.\ KCl)}$ and using a constant charge of 600 mC cm^{-2}, to achieve better control over the thickness of the films. Thus, films deposited using this methodology can have their thickness within a range of 300 to 400 nm, allowing better absorption of light without losses due to the high probability of recombination (for thicker films) or low indices of light absorption (for thinner films).[63,64]

2.4. Thermal treatment

In sequence, all samples were thermally treated in a glass cylinder of lead borosilicate (approximately 300 mL volume) composed of two parts so that it was possible to lightly rub them. Inside the cylinder, the samples remained between two crucibles each containing 0.1 g of selenium powder to maintain a controlled atmosphere rich in $Se_{(vapour)}$. In this process, a tube furnace with an Ar atmosphere was maintained at 1 atm and a flow of 1 mL min^{-1} released in a bubbler filled with mineral oil.[19]

2.5. Physical characterization

The morphological and structural characterization of the films were performed by high-resolution field (Zeiss Supra 35) scanning electron microscopy (SEM) and X-ray diffraction (XRD) (Rigaku DMax2500PC) with CuKα radiation and a sweep rate of 0.2° min^{-1}, respectively. To complement the characterization, Raman spectra were obtained under 532 nm excitation using an FT-Raman (Bruker MultiRAM) spectrometer coupled with a RamanScope III. It is important to mention that the laser power was adjusted to prevent damaging the surface of the samples. The composition was evaluated and elemental mapping performed by energy-dispersive X-ray spectroscopy (EDS) (FEI-XL30-FEG with Oxford Instruments Link detector ISIS 300), while the chemical environment was examined by X-ray photoelectron spectroscopy (XPS, Scienta Omicron, ESCA 2SR) with Al-Kα radiation (1486.7 eV). The spectra were calibrated with the C 1s peak at 284.6 eV, the line shape was adjusted with the GL function (30%) and for the baseline, the Shirley function was used. The counting and measurement of the size of particles were performed with the aid of ImageJ 1.8.0 software. The optical bandgap energy (E_g) determination was performed using an NIR-UV-Vis spectrometer with diffuse reflectance (Cary 5E spectrometer) by means of the following equations:[65]

$$\alpha = F(R) = (1 - R)^2/2R$$

$$(\alpha h\nu)^n = A(h\nu - E_g)$$

where $F(R)$ is the Kubelka–Munk function, R the absolute reflectance for a given value of $h\nu$, α the absorption coefficient, h the Planck constant, ν the frequency and n assumes the values of 2 or 2/3 for direct transition (allowed and forbidden, respectively) and 1/2 or 1/3 for indirect transition (allowed and forbidden, respectively).

2.6. Photoelectrochemical measurements

Photoelectrochemical measurements were performed using a 150 W xenon solar lamp simulator (Newport 66902) and an AM 1.0 lens as the light source, using a quartz window electrochemical cell with a 1 cm optical path between the window and the surface of the films. Because of the initial photocorrosion effect, the photocurrent transients were normalized to the current obtained from the linear sweep voltammetry curves of the respective films. The equation below was used to convert the potentials from the $Ag/AgCl/Cl^-_{(sat.\ KCl)}$ to the reversible hydrogen electrode (RHE) scale:[66]

$$E\ (vs.\ \mathrm{RHE}) = E_{appl.}\ (vs.\ Ag/AgCl/Cl^-_{(sat.\ KCl)}) + \mathrm{pH} \times 0.059\ \mathrm{V} + 0.197\ \mathrm{V}$$

The photoconversion can be calculated using the applied bias photon-to-current efficiency (ABPE), considering a faradaic efficiency of 100% and using the following equation:[63]

$$\mathrm{ABPE} = \frac{|J| \times (1.23\ - |E_{appl.}|) \times \eta_F}{P}$$

where J is the photocurrent density, $E_{appl.}$ is the applied potential, η_F is the faradaic efficiency, and P is the incident illumination power density (100 mW cm^{-2}). The interfacial properties between the electrode and the electrolyte were characterized by electrochemical impedance spectroscopy (EIS). The flat-band potential (E_{fb}), the energy of the band-edges, charge carrier density (N_A) and semiconductor type (n- or p-) were determined by Mott–Schottky analysis using the equation below.[67] The scanning proceeded from the open circuit potential to −0.40 V *vs.* $Ag/AgCl/Cl^-_{(sat.\ KCl)}$ by applying a sinusoidal excitation signal of 0.01 V_{rms} with a frequency of 5 kHz.

$$C_{sc}^{-2} = -2(\varepsilon_{sc}\varepsilon_0 A^2 e N_A)^{-1}\ [E - E_{fb} + (k_B T e^{-1})]$$

where C_{sc} is the capacitance of the space charge region of the semiconductor, ε_{sc} is the dielectric constant of the semiconductor (15 for Sb_2Se_3 (ref. 68)), ε_0 is the vacuum permittivity, A is the area, e is the elementary charge, N_A is the acceptor density (for p-type semiconductors), E is the applied potential, E_{fb} is the flat-band potential, k_B is the Boltzmann constant and T is the absolute temperature. These experiments were performed using the same support electrolyte used in the electrodepositions.

3. Results and discussion

3.1. Characterization of the structure, composition, and morphology

As mentioned in the Experimental section, the cobalt-modified Sb_2Se_3 films were electrodeposited from electrolytic baths with three different concentrations of the cobalt precursor (0.125, 0.500 and 1.250 mmol L^{-1} $CoSO_4$), creating proportions relative to the antimony concentration (Co : Sb) of 1 : 20, 1 : 5 and 1 : 2. Hereafter, the cobalt-modified Sb_2Se_3 films will be named as Co_Sb_2Se_3 (ratio between Co and Sb). After deposition, the films were thermally treated according to the procedure optimized and well-developed in our laboratory.[45,69,70] To evaluate the presence of bulk and surface secondary phases, the films were characterized by XRD and Raman spectroscopy, respectively. Fig. 1a shows the diffractograms of the samples under the different conditions, where it is observed that the main characteristic peaks of the orthorhombic pattern of Sb_2Se_3 were indexed. No additional peak related to the secondary phase of cobalt-compounds was observed in the diffractograms. A slight increase in the bulk crystallinity of the modified films is noted, compared to the unmodified film, upon decreasing the full width at half maximum (FWHM) of the (221) and (120) peaks of each film (peaks that presented good intensity without being distorted by background noise, and that were not affected by other XRD peaks from the secondary phases and substrate), as seen in Table 1. This fact may be related to the incorporation of Co in the film since some ions can help the grain growth, as observed by other authors.[71] To verify if there was any change in texturing during grain growth, the texture coefficient (TC) of the unaffected peaks observed in the XRD patterns was determined using the following equation[72]

$$\mathrm{TC}(hkl) = \frac{I(hkl)/I_0(hkl)}{\frac{1}{n}\sum_n I(hkl)/I_0(hkl)}$$

where I is the peak intensity corresponding to the hkl plane, I_0 is the peak intensity of the pattern (ICSD 85676) corresponding to the hkl plane, and n is the number of peaks used in the measurement. The relative texture coefficient (TC_{rel}) was obtained between the (120) and (020) planes due to its perpendicularity and can be seen in Table 1. Only a slight change in texture has been observed in cobalt-modified films and no significant tendency can be obtained from the data. This change may be a result of the deviation from the thermodynamic and kinetic processes involved in electrodeposition and consequent texturing, or even a result of the presence of secondary phases, as shown next.

It is possible to observe the presence of the secondary phases of hexagonal Se (h-Se) or Sb_2O_3 by means of the peaks at $2\theta = 30.3°$ and 32.7° for Co_Sb_2Se_3 1 : 5, and $2\theta = 28.4°$ and 30.3° for the Co_Sb_2Se_3 1 : 2 film (represented by the symbol "&" in the inset of Fig. 1a). It is worth mentioning that Sb_2O_3 has higher free Gibbs energy of formation compared to Sb_2Se_3 and, therefore, the growth of oxides on the film surface that is exposed to air is favoured.[42]

The Raman spectra of the electrodeposited films are shown in Fig. 1b. Some authors report that the principal peaks of Sb_2Se_3 are observed at 189 and 253 cm^{-1}, equivalent to the heteropolar Sb–Se and non-polar Sb–Sb bonds, respectively, while the peaks at 372 and 450 cm^{-1} correspond to Sb–Se bonds.[73] However, Shongalova *et al.* carried out a more detailed study on the Raman spectrum of Sb_2Se_3 in controlled atmospheres.[74] According to the authors, the peaks at *ca.* 253 and 450 cm^{-1} (observed in our data) are actually attributed to Sb_2O_3, which is spontaneously formed on the film surface due to the material's oxidation after exposure to air or caused by laser heating during Raman analysis. Comparing the relative intensities of the Raman peaks at 253 cm^{-1} (Sb_2O_3) and 189 cm^{-1} (Sb_2Se_3), shown in Table 1, we can argue that the presence of Co ions in the electrolytic bath favoured the growth of superficial antimony oxide since the ratio between these peak intensities increases as long as the concentration of Co in the bath is increased.

Table 1 also shows the atomic composition of the films determined by EDS, beyond the FWHM of the most intense peak

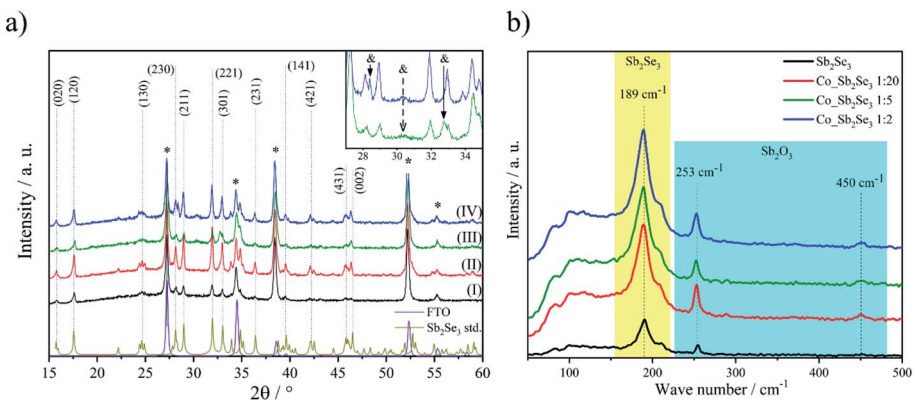

Fig. 1 (a) XRD patterns of the (I) unmodified, (II) Co_Sb_2Se_3 1 : 20, (III) Co_Sb_2Se_3 1 : 5 and (IV) Co_Sb_2Se_3 1 : 2 films. The SnO_2 (FTO, JCPDS 77-451) and Sb_2Se_3 (ICSD 85676) patterns are shown in the lower region of the graph for comparison. The inset highlights the extra peaks for the Co_Sb_2Se_3 1 : 5 and 1 : 2 films associated with the secondary phases; & = Sb_2O_3 (JCPDS 72-1854) or h-Se (JCPDS 86-2246 and 85-568). (b) Raman spectra for electrodeposited unmodified and cobalt-modified Sb_2Se_3 films.

Table 1 Additional information on the XRD patterns, Raman intensity and atomic composition of the unmodified and cobalt-modified Sb_2Se_3 films

	FWHM[a]				Atomic %			
Films	(221)	(120)	I (253 cm^{-1})/I (189 cm^{-1})[b]	TC_{rel} (120)/(020)	Sb	Se	Se/Sb	Co
Sb_2Se_3	0.28	0.24	0.35	1.01	39.7	60.3	1.5	n.d.
Co_Sb_2Se_3 1 : 20	0.20	0.21	0.55	1.00	36.8	62.2	1.7	1.1
Co_Sb_2Se_3 1 : 5	0.20	0.21	0.57	0.86	35.3	63.6	1.8	1.0
Co_Sb_2Se_3 1 : 2	0.20	0.22	0.64	0.88	36.8	62.4	1.7	0.8

n.d. = not detected.[a] FWHM for the (221) and (120) planes of the Sb_2Se_3 phase. [b] The Raman peaks at 253 and 189 cm^{-1} are attributed to the superficial-Sb_2O_3 and Sb_2Se_3 phases, respectively.

XRD pattern of Sb_2Se_3, and the ratio between the Raman intensity for the peaks at 253 and 189 cm^{-1} (attributed to the superficial-Sb_2O_3 and Sb_2Se_3 phases, respectively). Observing the composition data, it is possible to note that there was preferential incorporation of Se for films deposited from baths with Co ions, and this incorporation was higher for the Co_Sb_2Se_3 1 : 5 film (the individual sample data can be seen in Fig. S1†). However, the concentration of Co in the film, as expected, was low in relation to the other elements, because the deposition potential of this metal is more negative than the potential for Sb_2Se_2 deposition.[75] It is also worth mentioning that, due to the very low concentration of Co, we failed to determine the elemental distribution of this metal on the film surface by EDS or XPS, which is a common fact for this level of composition.[20]

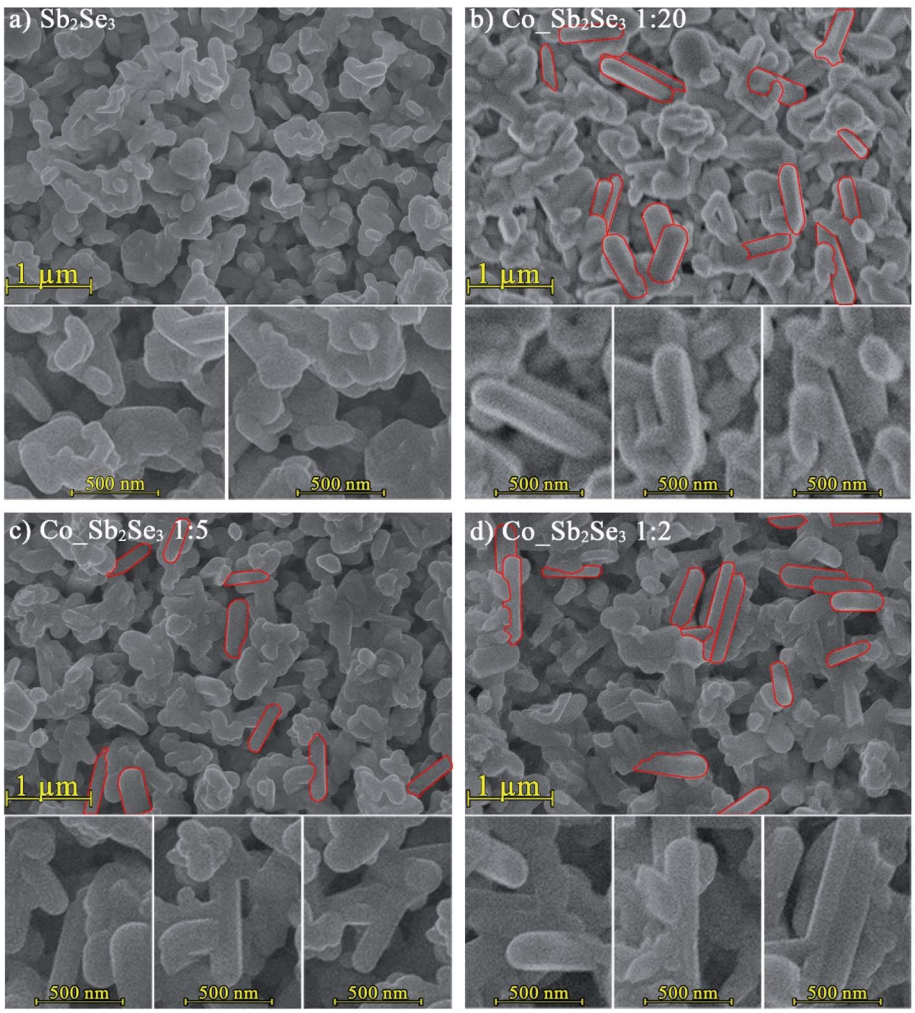

Fig. 2 Micrographs obtained by SEM of the film's surface with 50k magnification: (a) unmodified film, and Co_Sb_2Se_3 films obtained from electrolytic baths with Co : Sb ratios of (b) 1 : 20, (c) 1 : 5, and (d) 1 : 2. The red contours show the formation of rod-shaped structures on the surface of some films (non-contoured images can be seen in Fig. S2b†).

At this point, it is interesting to analyse how the change in composition, the crystallinity of the bulk and the presence of superficial secondary phases affect the morphology of the films. So, the morphology was characterized by SEM and the micrographs obtained are presented in Fig. 2. It is possible to observe that all the films were homogeneous and uniform (Fig. S2 and S3†). However, the presence of well-defined rod-shaped structures was observed in some films (as highlighted with red contours in Fig. 2 and below the image), showing particle sizes ranging between 626 and 1046 nm (Fig. S4†). The formation of these microstructures can be correlated with the excess Se, as was also observed by Khan *et al.* for films obtained by physical vapour deposition at different deposition temperatures.[76] According to the authors, the anisotropic cleavage of the Sb_2Se_3 structure allows its 1D-ribbons to be broken from the bulk (held together by van der Waals forces) and favours the formation of rods. It is also possible that the incorporation of Co ions has occurred in the GBs, causing the same effects as observed for the Se-rich material. A similar behaviour had already been observed in our previous work with Fe doping[45] and, as discussed, the introduction of foreign ions may also have altered the phenomena of nucleation and growth of the films, resulting in the formation of rod-shaped structures and Se-rich samples.

3.2. Optoelectronic and electrochemical characterization

Fig. 3 shows the curves of $(\alpha h\nu)^n$ *vs.* photon energy within a range of 1.00 to 1.55 eV. From data obtained from GW calculations, Vadapoo *et al.* confirmed that Sb_2Se_3 has allowed indirect and direct transitions.[77] Therefore, the Tauc plot ($(\alpha h\nu)^n = 0$) for both transitions presented linear behaviour, as shown in Fig. 3a and b. The optical bandgap energy (E_g) data obtained are presented in Table 2. From this study, it was possible to conclude that the low cobalt incorporation in the structure did not significantly affect the E_g, exhibiting values of 1.16 ± 0.01 and 1.21 ± 0.01 eV for indirect and direct transitions, respectively. The absence of change in the bandgap of the films can also be considered as evidence that the Co^{2+} ions were not incorporated into the bulk Sb_2Se_3 structure. Thus, these ions can be at the GBs, not affecting the optical properties of the bulk, which are responsible for the greater part of the optical absorption of the film. Using the same method, several studies in the literature have reported permitted transitions of Sb_2Se_3 thin films within the range of 1.0–2.1 eV.[77] This also shows that both values agree with those obtained in the literature.

Fig. 4 shows the Mott–Schottky graphs of the unmodified and cobalt-modified films with their respective carrier densities (N_A) and the flat-band potential (E_{fb}). These values are presented in Table 2.

From the obtained data, it can be observed that the cobalt incorporated into the film did not affect the order of magnitude of the N_A and the semiconductor conductivity type since the angular coefficients of the films indicated a p-type conductivity in all cases.[78] The unmodified and Co_Sb_2Se_3 1 : 20 films showed E_{fb} very close to the energy of the VBM determined by

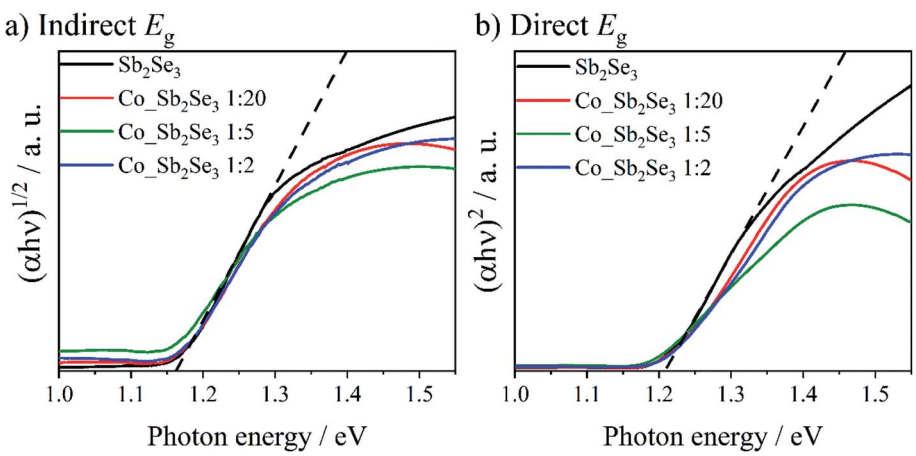

Fig. 3 Graphs of $(\alpha h\nu)^n$ *vs.* photon energy. The value of linear extrapolation on the *x*-axis is equal to the (a) indirect and (b) direct allowed bandgap (E_g).

Table 2 Additional information on the optoelectronic and photoelectrochemical properties of the unmodified and cobalt-modified Sb_2Se_3 films

Films	E_g ind./eV	E_g dir./eV	N_A/cm^{-3}	E_{fb}[a]/eV *vs.* vacuum	j[b]/μA cm^{-2}
Sb_2Se_3	1.17	1.21	2.5×10^{17}	−5.3	200.8
Co_Sb_2Se_3 1 : 20	1.16	1.21	6.6×10^{17}	−5.2	209.2
Co_Sb_2Se_3 1 : 5	1.16	1.19	4.0×10^{17}	−4.7	146.1
Co_Sb_2Se_3 1 : 2	1.16	1.22	2.8×10^{17}	−4.9	178.8

[a] [Energy *vs.* vacuum] = $-e$ [*E vs.* SHE] − 4.44 eV.[43] [b] At −0.315 V *vs.* Ag/AgCl/$Cl^-_{(sat.\ KCl)}$, the hydrogen reduction potential in 0.5 mol L^{-1} Na_2SO_4/H_2SO_4 – pH 2.

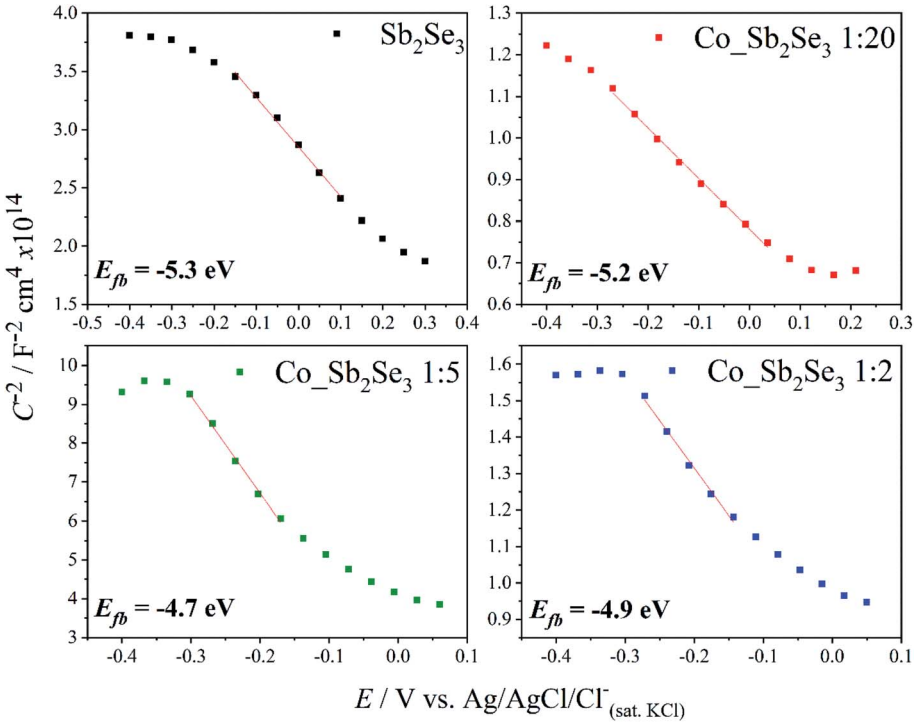

Fig. 4 Mott–Schottky plots for the unmodified and cobalt-modified Sb_2Se_3 films applying a sinusoidal excitation (V_{rms}) of 0.01 V with a frequency of 5 kHz.

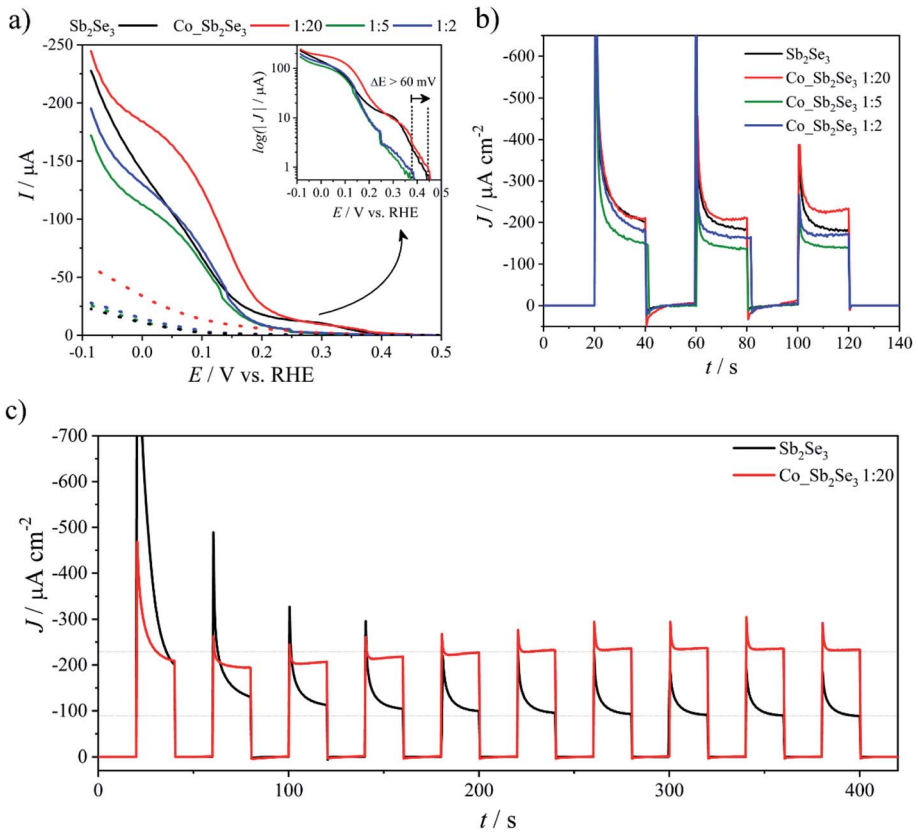

Fig. 5 (a) Linear voltammetry curves at 50 mV s^{-1} in the dark (dotted lines) and under solar illumination (solid lines; 1 sun = 100 mW cm^{-1}, A.M. 1.0 lens). (b) Photocurrent transients at the potential of hydrogen reduction, 0 V *vs.* RHE, over 140 and (c) 420 seconds for the unmodified and Co_Sb_2Se_3 1 : 20 films.

Liu *et al.*,[42] using UPS, *i.e.*, −5.35 eV, which is expected for lightly doped p-type semiconductors.[79–81] In contrast, the E_{fb} for the Co_Sb_2Se_3 1 : 5 and 1 : 2 films was shifted to higher values of energy than the ones for the unmodified and Co_Sb_2Se_3 1 : 20 films. This shift, related to the upshift of the Fermi level, can be evidence that the Co^{2+} ions are being incorporated into the GBs, probably in the interstitial position (Co_i) between the Sb_2Se_3 1D-ribbons, causing an n-type inversion at the GBs; a very similar behaviour was observed by Tang *et al.* when studying the grain boundary inversion by interstitial incorporation of Cu into Sb_2Se_3 film.[20] As Co^{2+} and Cu^{2+} ions have similar charges and ionic radii, we expect that a similar effect to that observed by these authors occurs in our cobalt-modified films.

3.3. Photoelectrochemical characterization

The photocurrent density (j) values were obtained by linear voltammetry in the dark and under illumination (Fig. 5a), in an electrolytic solution of 0.5 mol L^{-1} Na_2SO_4/H_2SO_4 – pH 2, and are listed in Table 2. In this figure, a slight shift in the onset potential (E_{onset}) of the HER can be noted. For the unmodified and Co_Sb_2Se_3 1 : 20 films, the HER started at about 460 mV *vs.* RHE, while it initiated at about 380 mV for the Co_Sb_2Se_3 1 : 5 and 1 : 2 films. In the latter cases, the photoactivity of the films may have been harmed due to the formation of a thicker secondary phase layer on the film surface when compared to the unmodified and Co_Sb_2Se_3 1 : 20 films. This layer can create some surface states that act as recombination centres. As was noted before, the electrodeposition baths with higher cobalt concentrations contributed to the formation of the secondary phases, which may lead to this greater overpotential. In addition, the formation of these secondary phases also caused a decreasing photocurrent, reaching values of 146.1 and 178.8 μA cm^{-2} for the Co_Sb_2Se_3 1 : 5 and 1 : 2 films, respectively, compared to higher initial values of 200.8 and 209.2 μA cm^{-2} for the unmodified and Co_Sb_2Se_3 1 : 20 films, respectively. When evaluating the photocurrent transients (Fig. 5b), a slight increase in the photocurrent values for the Co_Sb_2Se_3 1 : 20 film is observed as the number of transient cycles is increased. The other cobalt-modified films remain more stable, while the unmodified film suffers from the typical initial photocorrosion process.[35] To better evaluate this behaviour, the experiment was repeated under the same conditions over several transient cycles for the unmodified and Co_Sb_2Se_3 1 : 20 films, as seen in Fig. 5c. In addition, XPS analysis of the Co_Sb_2Se_3 1 : 20 film surface was performed before and after the photoelectrochemical experiments, to observe the likely Sb_2O_3 formation on the film. The spectra can be seen in Fig. 6. The formation of Sb_2O_3 and its associated effects will be discussed later.

In Fig. 5c, observing the decay profile of the photocurrent immediately after the light is turned on, we can see that the unmodified film shows a higher initial photocurrent when compared to that of the Co_Sb_2Se_3 1 : 20 film, which quickly decreases in the first few seconds when the electrode is illuminated. It is known that the current decay during the time that the electrode remains illuminated is due to interface recombination. Generally, these recombinations are caused by the

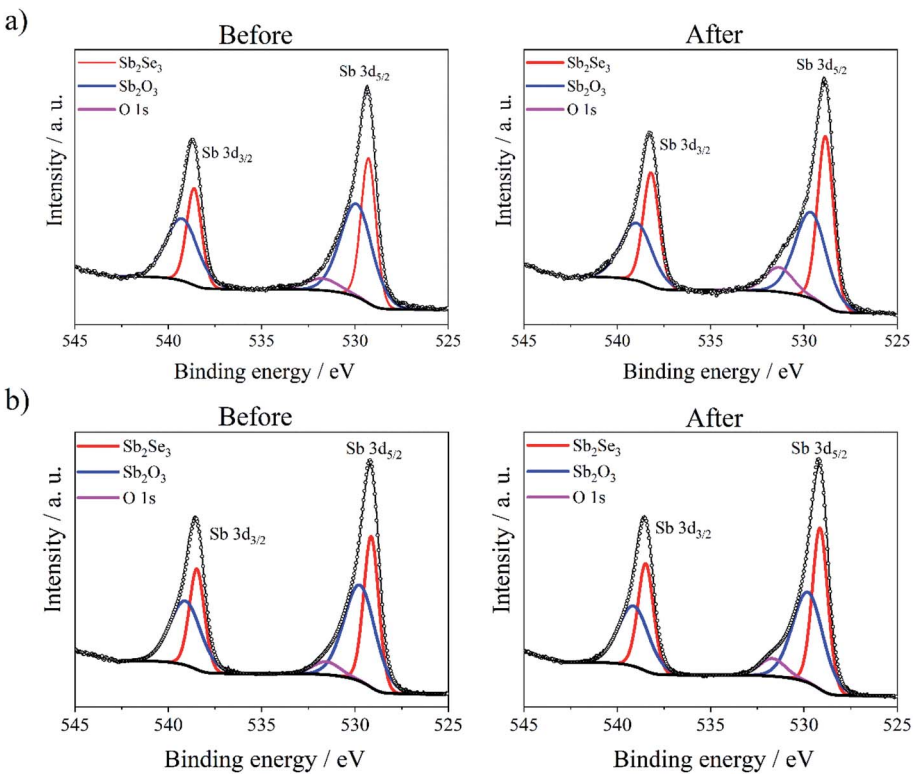

Fig. 6 XPS spectra of Sb 3d and O 1s before and after photoelectrochemical analysis for the (a) Co_Sb_2Se_3 1 : 20 and (b) unmodified films.

majority carriers being captured by minority carriers that are trapped in the surface states.[82] Thus, this behaviour indicates a higher rate of recombination at the interface for the unmodified film. Therefore, it is possible to observe that the modification with Co allowed the decrease in recombination rates and consequent increase in the photocurrent. This can be noticed from the greater photoconversion efficiency (ABPE) when comparing these films. Fig. S5† shows an increase in ABPE for the Co_Sb_2Se_3 1 : 20 film between 0.2 and 0 V *vs.* RHE, reaching a maximum value of ~2.5%.

Another interesting feature observed in Fig. 5c is that the photocurrent for the Co_Sb_2Se_3 1 : 20 film firstly decreases from the first to the second transient cycle and then increases from the second to the subsequent cycles. The photocurrent reaches a quasi-steady-state and stabilizes at ~226.5 μA cm^{-2} after 300 seconds, *i.e.*, a value 2.5 times higher than that of the unmodified film in the same period. The decay profile of the photocurrent transients clearly shows that there was a reduction in the recombination rates from the charges accumulated in the surface states for the Co modified film. In contrast, for the unmodified film, this photocurrent just decreases until stabilizing at a value 44% lower than the initial value, after 200 seconds.

To explain this behaviour, we believe that the decrease in photocurrent is caused by the initial photocorrosion of the films and, based on the first transient cycle in Fig. 5c, we would argue that the photocorrosion of the unmodified film is faster in comparison with that of the Co_Sb_2Se_3 1 : 20 film. The lower rate of photocorrosion for the former film may be associated with the n-type inversion at the GBs, promoted by the Co_i, which likely decreases the charge accumulation and improves the carriers transfer. As mentioned before, a very similar behaviour was observed by Tang *et al.* with interstitial incorporation of Cu into Sb_2Se_3 film.[20] In addition, this photodegradation of the film creates a thin layer of Sb_2O_3, which inhibits the subsequent photocorrosion and passivates some surface defects, a phenomenon that causes the stabilization of the photocurrent, as was seen on both films. The presence of Sb_2O_3 can be seen in the XPS spectra of Fig. 6 by means of the Sb–O doublet peaks at ~530 eV. It is possible to observe an increase in the

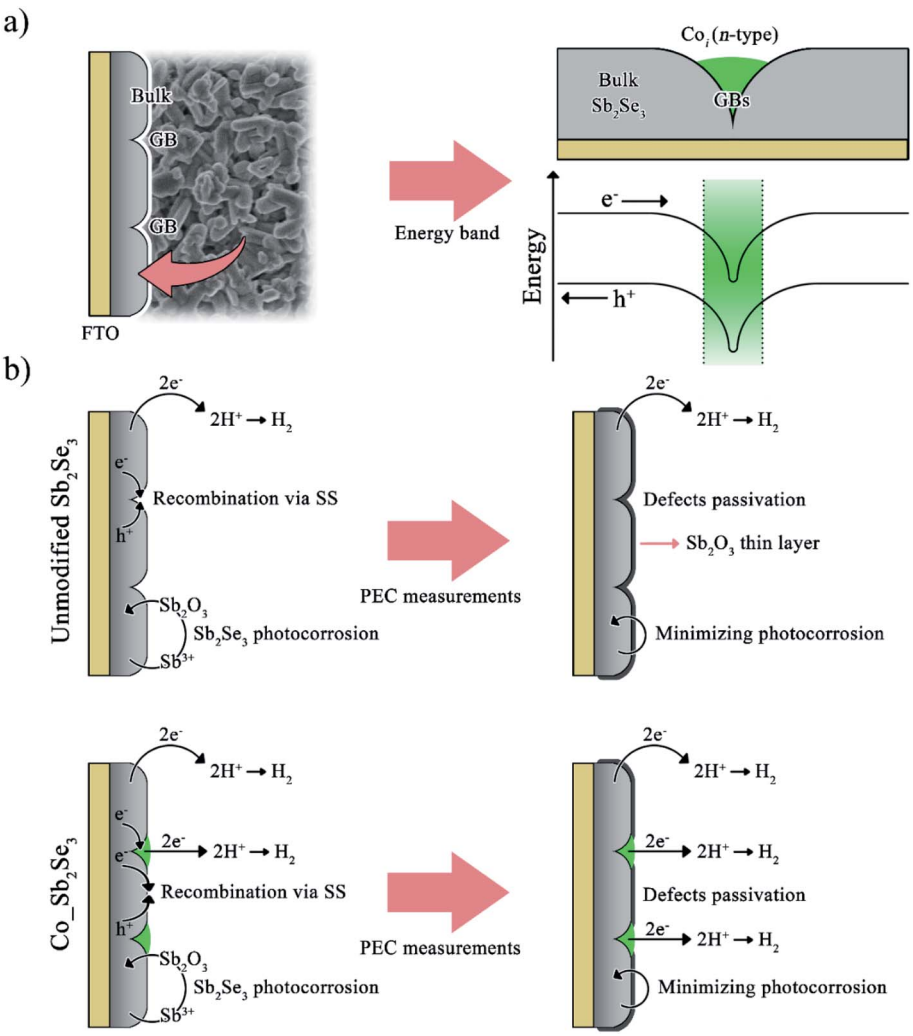

Fig. 7 Schematic representation of surface passivation associated with the grain boundary inversion. (a) The energetic effect caused by the GBs and (b) the mechanism of photocorrosion and the passivation of the films.

area below the peak corresponding to O 1s after photoelectrochemical analysis; the Co_Sb_2Se_3 1 : 20 film showed an increase of 1.7 times, while the unmodified film presented a lower increase of 1.2 times (Table S1†). This shows that Sb_2O_3 is formed naturally on the film surfaces, but this effect is intensified as the films are subjected to photoelectrochemical analysis. The oxide formation comes from the increase of the interfacial pH during cathodic scanning[83] according to the following equations:

$$2H_2O_{(l)} + 4e^- \rightarrow H_{2(g)} + 2OH^-_{(aq.)}$$

$$Sb_2Se_{3(s)} + 4OH^-_{(aq.)} \rightarrow 2Sb(OH)^+_2 + 3Se^{2-}_{(aq.)}$$

$$2Sb(OH)^+_2 + 2OH^-_{(aq.)} \rightarrow Sb_2O_{3(s)} + 3H_2O_{(l)}$$

Since Sb_2O_3 is only soluble in strongly acidic or basic medium,[84] this oxide will likely precipitate on the Sb_2Se_3 surface. The surface passivation associated with the grain boundary inversion (GBI) makes the photocurrent for the modified films increase slightly after the photocorrosion period (after the second transient cycle). Fig. 7 shows the schematic effect discussed above: Fig. 7a presents the energetic effect caused by the GBI, which enhances the charge separation at the GB region; Fig. 7b shows the mechanism of photocorrosion and passivation of the films.

Based on the abovementioned pieces of evidence, we may summarize that cobalt-modification improves the photoactivity and initial photostability of the Sb_2Se_3 films, making them potential photocathodes for PEC cells applied to hydrogen production from water splitting after addition of protecting and catalytic layers. In fact, some studies have also reported an improvement in the electron transfer at the interface[85,86] and excellent electrochemical stability[87] of cobalt-modified semiconductor materials in the HER. In future studies, it may be interesting to examine the effect of co-catalyst layers and heterostructures on this kind of photocathode to enhance its photocurrent even more.

4. Conclusions

In short, cobalt-modification of Sb_2Se_3 films showed interesting effects on the photoelectrocatalytic properties of this material towards the HER. Although the crystalline structure and optoelectronic properties of the films remained unchanged, the presence of Co allowed the modification of GBs. For the Co_Sb_2Se_3 1 : 20 film, interstitial Co may have caused the formation of regions associated with an n-type inversion at the GBs. As a result, the density of accumulated charges on the film surface decreased and the charge transfer was improved. After photodegradation of the unmodified and modified Sb_2Se_3 films during photoelectrochemical analysis, a thin layer of Sb_2O_3 is formed and defects on the film surface are likely passivated. Again, the presence of Co^{2+} ions in GBs allowed better initial stability and an increase in the photocurrent value up to 2.5 times compared to the unmodified film, over the same period. In this work we have shown Sb_2Se_3 films modified with Co that were grown by an easy synthetic method; greater photocurrent and photostability were demonstrated, which make this material promising for application in photoelectrochemical devices for hydrogen production.

Conflicts of interest

There are no conflicts to declare.

Acknowledgements

This work was supported by the National Council of Technological and Scientific Development (CNPq) and the São Paulo Research Foundation (FAPESP), grant #2017/21365-8, grant #2018/03156-5, grant #2018/16401-8, CEPID grant #2013/07296-2, FAPESP/SHELL grant #2017/11986-5, CAPES – Finance Code 001.

References

1 Y. Zhao, Z. Yang, Y. Zhang, J. Lin, X. Guo, Z. Ke, P. Hu, G. Wang, Y. Yan and K. Sun, *J. Phys. Chem. C*, 2014, **114**, 14238–14245.
2 J. Pan, S. Li, Y. Liu, W. Ou, H. Li, W. Zhao, J. Wang, C. Song, Y. Zheng and C. Li, *Chem. Eng. J.*, 2020, **382**, 122813.
3 E. M. Chen, L. Williams, A. Olvera, C. Zhang, M. Zhang, G. Shi, J. T. Heron, L. Qi, L. J. Guo, E. Kioupakis and P. F. P. Poudeu, *Chem. Sci.*, 2018, **9**, 5405–5414.
4 J. de Wild, F. Babbe, E. V. C. Robert, A. Redinger and P. J. Dale, *IEEE J. Photovolt.*, 2018, **8**, 299–304.
5 W. Septina, S. Ikeda, Y. Iga, T. Harada and M. Matsumura, *Thin Solid Films*, 2014, **550**, 700–704.
6 F. W. de Souza Lucas and A. Zakutayev, *APL Mater.*, 2018, **6**, 084501.
7 F. Willian de Souza Lucas, H. Peng, S. Johnston, P. C. Dippo, S. Lany, L. H. Mascaro and A. Zakutayev, *J. Mater. Chem. A*, 2017, **5**, 21986–21993.
8 A. Mavlonov, T. Razykov, F. Raziq, J. Gan, J. Chantana, Y. Kawano, T. Nishimura, H. Wei, A. Zakutayev, T. Minemoto, X. Zu, S. Li and L. Qiao, *Sol. Energy*, 2020, **201**, 227–246.
9 J. Ma, Y. Wang, Y. Wang, Q. Chen, J. Lian and W. Zheng, *J. Phys. Chem. C*, 2009, **113**, 13588–13592.
10 L. Zhang, Y. Li, C. Li, Q. Chen, Z. Zhen, X. Jiang, M. Zhong, F. Zhang and H. Zhu, *ACS Nano*, 2017, **11**, 12753–12763.
11 G. Ghosh, *J. Phase Equilib.*, 1993, **14**, 753–763.
12 C. E. Patrick and F. Giustino, *Adv. Funct. Mater.*, 2011, **21**, 4663–4667.
13 C. Chen, W. Li, Y. Zhou, C. Chen, M. Luo, X. Liu, K. Zeng, B. Yang, C. Zhang, J. Han and J. Tang, *Appl. Phys. Lett.*, 2015, **107**, 043905.
14 K. U. Isah, J. A. Yabagi, U. Ahmadu, M. I. Kimpa, M. G. Z. Kana and A. A. Oberafo, *IOSR J. Appl. Phys.*, 2013, **2**, 14–19.

15 I. L. Validžić, M. Mitrić, N. D. Abazović, B. M. Jokić, A. S. Milošević, Z. S. Popović and F. R. Vukajlović, *Semicond. Sci. Technol.*, 2014, **29**, 035007.

16 B. Yang, L. Wang, J. Han, Y. Zhou, H. Song, S. Chen, J. Zhong, L. Lv, D. Niu and J. Tang, *Chem. Mater.*, 2014, **26**, 3135–3143.

17 Y. Zhou, L. Wang, S. Chen, S. Qin, X. Liu, J. Chen, D.-J. Xue, M. Luo, Y. Cao, Y. Cheng, E. H. Sargent and J. Tang, *Nat. Photonics*, 2015, **9**, 409–415.

18 C. Chen, D. C. Bobela, Y. Yang, S. Lu, K. Zeng, C. Ge, B. Yang, L. Gao, Y. Zhao, M. C. Beard and J. Tang, *Front. Optoelectron.*, 2017, **10**, 18–30.

19 M. B. Costa, F. W. de Souza Lucas and L. H. Mascaro, *ChemElectroChem*, 2017, **4**, 2507–2514.

20 C. Chen, K. Li, S. Chen, L. Wang, S. Lu, Y. Liu, D. Li, H. Song and J. Tang, *ACS Energy Lett.*, 2018, **3**, 2335–2341.

21 K. Zeng, D.-J. Xue and J. Tang, *Semicond. Sci. Technol.*, 2016, **31**, 1–13.

22 Z. Li, X. Liang, G. Li, H. Liu, H. Zhang, J. Guo, J. Chen, K. Shen, X. San, W. Yu, R. E. I. Schropp and Y. Mai, *Nat. Commun.*, 2019, **10**, 125.

23 X. Wen, C. Chen, S. Lu, K. Li, R. Kondrotas, Y. Zhao, W. Chen, L. Gao, C. Wang, J. Zhang, G. Niu and J. Tang, *Nat. Commun.*, 2018, **9**, 2179.

24 K. Li, S. Wang, C. Chen, R. Kondrotas, M. Hu, S. Lu, C. Wang, W. Chen and J. Tang, *J. Mater. Chem. A*, 2019, **7**, 9665–9672.

25 T. D. C. Hobson, L. J. Phillips, O. S. Hutter, H. Shiel, J. E. N. Swallow, C. N. Savory, P. K. Nayak, S. Mariotti, B. Das, L. Bowen, L. A. H. Jones, T. J. Featherstone, M. J. Smiles, M. A. Farnworth, G. Zoppi, P. K. Thakur, T.-L. Lee, H. J. Snaith, C. Leighton, D. O. Scanlon, V. R. Dhanak, K. Durose, T. D. Veal and J. D. Major, *Chem. Mater.*, 2020, **32**, 2621–2630.

26 G.-X. Liang, Y.-D. Luo, S. Chen, R. Tang, Z.-H. Zheng, X.-J. Li, X.-S. Liu, Y.-K. Liu, Y.-F. Li, X.-Y. Chen, Z.-H. Su, X.-H. Zhang, H.-L. Ma and P. Fan, *Nano Energy*, 2020, **73**, 104806.

27 Y.-D. Luo, R. Tang, S. Chen, J.-G. Hu, Y.-K. Liu, Y.-F. Li, X.-S. Liu, Z.-H. Zheng, Z.-H. Su, X.-F. Ma, P. Fan, X.-H. Zhang, H.-L. Ma, Z.-G. Chen and G.-X. Liang, *Chem. Eng. J.*, 2020, **393**, 124599.

28 R. Tang, Z.-H. Zheng, Z.-H. Su, X.-J. Li, Y.-D. Wei, X.-H. Zhang, Y.-Q. Fu, J.-T. Luo, P. Fan and G.-X. Liang, *Nano Energy*, 2019, **64**, 103929.

29 G.-X. Liang, Z.-H. Zheng, P. Fan, J.-T. Luo, J.-G. Hu, X.-H. Zhang, H.-L. Ma, B. Fan, Z.-K. Luo and D.-P. Zhang, *Sol. Energy Mater. Sol. Cells*, 2018, **174**, 263–270.

30 C. Chen, L. Wang, L. Gao, D. Nam, D. Li, K. Li, Y. Zhao, C. Ge, H. Cheong, H. Liu, H. Song and J. Tang, *ACS Energy Lett.*, 2017, **2**, 2125–2132.

31 K. T. Fountaine, H. J. Lewerenz and H. A. Atwater, *Nat. Commun.*, 2016, **7**, 1–9.

32 M. S. Ahmad, A. K. Pandey, N. A. Rahim, S. Shahabuddin and S. K. Tyagi, *Ceram. Int.*, 2018, **44**, 18444–18449.

33 P. Liang, L. Li, C. Liu, W. Wang, H. Zhang, N. Mitsuzaki and Z. Chen, *Thin Solid Films*, 2018, **666**, 161–171.

34 Q. Zeng, J. Li, L. Li, J. Bai, L. Xia and B. Zhou, *Appl. Catal., B*, 2017, **217**, 21–29.

35 C. Jiang, S. J. A. Moniz, A. Wang, T. Zhang and J. Tang, *Chem. Soc. Rev.*, 2017, **46**, 4645–4660.

36 H. Lee, W. Yang, J. Tan, Y. Oh, J. Park and J. Moon, *ACS Energy Lett.*, 2019, **4**, 995–1003.

37 J. Tan, W. Yang, Y. Oh, H. Lee, J. Park, R. Boppella, J. Kim and J. Moon, *Adv. Energy Mater.*, 2019, **9**, 1900179.

38 W. Yang, J. H. Kim, O. S. Hutter, L. J. Phillips, J. Tan, J. Park, H. Lee, J. D. Major, J. S. Lee and J. Moon, *Nat. Commun.*, 2020, **11**, 861.

39 J. Park, W. Yang, J. Tan, H. Lee, J. W. Yun, S. G. Shim, Y. S. Park and J. Moon, *ACS Energy Lett.*, 2020, **5**, 136–145.

40 R. R. Prabhakar, W. Septina, S. Siol, T. Moehl, R. Wick-Joliat and S. D. Tilley, *J. Mater. Chem. A*, 2017, **5**, 23139–23145.

41 J. Tan, W. Yang, Y. Oh, H. Lee, J. Park and J. Moon, *ACS Appl. Mater. Interfaces*, 2018, **10**, 10898–10908.

42 X. Liu, J. Chen, M. Luo, M. Leng, Z. Xia, Y. Zhou, S. Qin, D. Xue, L. Lv, H. Huang, D. Niu and J. Tang, *ACS Appl. Mater. Interfaces*, 2014, **6**, 10687–10695.

43 R. Beranek, *Adv. Phys. Chem.*, 2011, **2011**, 1–20.

44 D. Sobha Jayakrishnan, in *Corrosion Protection and Control Using Nanomaterials*, ed. V. S. Saj and R. Cook, Woodhead Publishing, New Delhi, 1st edn, 2012, pp. 86–125.

45 M. B. Costa, F. W. de Souza Lucas and L. H. Mascaro, *J. Solid State Electrochem.*, 2018, **22**, 1557–1562.

46 Y.-S. Hu, A. Kleiman-Shwarsctein, A. J. Forman, D. Hazen, J.-N. Park and E. W. McFarland, *Chem. Mater.*, 2008, **20**, 3803–3805.

47 A. E.-H. B. Kashyout, E.-Z. Ahmed, T. Meaz, M. Nabil and M. Amer, *Alexandria Eng. J.*, 2014, **53**, 731–736.

48 A. S. M. S. Rahman, M. A. Islam and K. M. Shorowordi, *Procedia Eng.*, 2015, **105**, 679–685.

49 N. R. Mathews, J. T. Benítez, F. Paraguay-Delgado, M. Pal and L. Huerta, *J. Mater. Sci.: Mater. Electron.*, 2013, **24**, 4060–4067.

50 F. Jiang, S. Li, C. Ozaki, T. Harada and S. Ikeda, *Sol. RRL*, 2018, **2**, 1700205.

51 Y. Li, Y. Zhou, Y. Zhu, C. Chen, J. Luo, J. Ma, B. Yang, X. Wang and Z. Xia, *Appl. Phys. Lett.*, 2016, **109**, 1–6.

52 R. Tang, X. Wang, C. Jiang, S. Li, W. Liu, H. Ju, S. Yang, C. Zhu and T. Chen, *ACS Appl. Mater. Interfaces*, 2018, **10**, 30314–30321.

53 J. Li, B. Wang, F. Liu, J. Yang, J. Li, J. Liu, M. Jia, Y. Lai and Y. Liu, *Electrochim. Acta*, 2011, **56**, 8597–8602.

54 R. Jin, Z. Liu, L. Yang, J. Liu, Y. Xu and G. Li, *J. Alloys Compd.*, 2013, **579**, 209–217.

55 S. Gautam, A. Thakur, S. K. Tripathi and N. Goyal, *J. Non-Cryst. Solids*, 2007, **353**, 1315–1321.

56 A. Alemi, Y. Hanifehpour, S. W. Joo and B. Min, *Phys. B*, 2011, **406**, 3831–3835.

57 Y. Hanifehpour, S. W. Joo and B. Min, *Nanoscale Res. Lett.*, 2013, **8**, 1–8.

58 D. Kutyła, K. Kołczyk and P. Zabi, *J. Electrochem. Soc.*, 2017, **164**, 700–706.

59 R. Mani, K. Vivekanandan and K. Vallalperuman, *J. Mater. Sci.: Mater. Electron.*, 2017, **28**, 4396–4402.

60 J. Li, Y. Peng, X. Qian and J. Lin, *Appl. Surf. Sci.*, 2018, **452**, 437–442.

61 X. Qiao, S. Liao, R. Zheng, Y. Deng, H. Song and L. Du, *ACS Sustainable Chem. Eng.*, 2016, **4**, 4131–4136.

62 A. I. Carim, F. H. Saadi, M. P. Soriaga and N. S. Lewis, *J. Mater. Chem. A*, 2014, **2**, 13835–13839.

63 Z. Chen, H. N. Dinh and E. Miller, *Photoelectrochemical Water Splitting: Standards, Experimental Methods, and Protocols*, Springer-Verlag New York, New York, 1st edn, 2013.

64 A. Ahnood, H. Zhou, Y. Suzuki, R. Sliz, T. Fabritius, A. Nathan and G. A. J. Amaratunga, *Nanoscale Res. Lett.*, 2015, **10**, 486.

65 M. Nowak, B. Kauch and P. Szperlich, *Rev. Sci. Instrum.*, 2009, **80**, 1–3.

66 J. Park, W. Yang, Y. Oh, J. Tan, H. Lee, R. Boppella and J. Moon, *ACS Energy Lett.*, 2019, **4**, 517–526.

67 K. Gelderman, L. Lee and S. W. Donne, *J. Chem. Educ.*, 2007, **84**, 685.

68 O. Madelung, *Semiconductors: Data Handbook*, Springer, New York, 3rd edn, 2004.

69 F. W. de Souza Lucas, A. W. Welch, L. L. Baranowski, P. C. Dippo, L. H. Mascaro and A. Zakutayev, in *2015 IEEE 42nd Photovoltaic Specialist Conference (PVSC)*, IEEE, 2015, pp. 1–5.

70 M. B. Costa, F. W. S. Lucas and L. H. Mascaro, *ChemElectroChem*, 2019, **6**, 2937–2944.

71 T. Nakada, Y. Honishi, Y. Yatsushiro and H. Nakakoba, in *2011 37th IEEE Photovoltaic Specialists Conference*, IEEE, 2011, pp. 003527–003531.

72 Y. Wang, W. Tang and L. Zhang, *J. Mater. Sci. Technol.*, 2015, **31**, 175–181.

73 J. Yang, Y. Lai, Y. Fan, Y. Jiang, D. Tang, L. Jiang, F. Liu and J. Li, *RSC Adv.*, 2015, **5**, 85592–85597.

74 A. Shongalova, M. R. Correia, B. Vermang, J. M. V. Cunha, P. M. P. Salomé and P. A. Fernandes, *MRS Commun.*, 2018, **8**, 1–6.

75 *Handbook of Electrochemistry*, ed. C. Zoski, Elsevier Science, New Mexico, 1st edn, 2007.

76 M. D. Khan, M. Aamir, M. Sohail, M. Sher, J. Akhtar, M. A. Malik and N. Revaprasadu, *Sol. Energy*, 2018, **169**, 526–534.

77 R. Vadapoo, S. Krishnan, H. Yilmaz, C. Marin and I. Antimony, *Phys. Status Solidi B*, 2011, **248**, 700–705.

78 K. Gelderman, L. Lee and S. W. Donne, *J. Chem. Educ.*, 2007, **84**, 685.

79 P. Y. Yu and M. Cardona, *Fundamentals of Semiconductors: Physics and Materials Properties*, Springer Berlin Heidelberg, Berlin, Heidelberg, 4th edn, 2010.

80 M. Grundmann, *The Physics of Semiconductors: An Introduction Including Nanophysics and Applications*, Springer, Berlin, 3rd edn, 2010.

81 S. M. Sze and K. K. Ng, *Physics of Semiconductor Devices*, John Wiley & Sons, New York, 3rd edn, 2007.

82 L. M. Peter, *Chem. Rev.*, 1990, **90**, 753–769.

83 E. B. Carneiro-Neto, M. C. Lopes and E. C. Pereira, *J. Electroanal. Chem.*, 2016, **765**, 92–99.

84 M. D. Larrañaga, R. J. Lewis and R. A. Lewis, *Hawley's Condensed Chemical Dictionary*, Wiley, Hoboken, 16th edn, 2016.

85 Q. Xiong, X. Zhang, H. Wang, G. Liu, G. Wang, H. Zhang and H. Zhao, *ChemComm*, 2018, **54**, 3859–3862.

86 Q. Xiong, Y. Wang, P.-F. Liu, L.-R. Zheng, G. Wang, H.-G. Yang, P.-K. Wong, H. Zhang and H. Zhao, *Adv. Mater.*, 2018, **30**, 1–7.

87 P. P. Patel, O. I. Velikokhatnyi, S. D. Ghadge, P. J. Hanumantha, M. K. Datta, R. Kuruba, B. Gattu, P. M. Shanthi and P. N. Kumta, *Int. J. Hydrogen Energy*, 2018, **43**, 7855–7871.